Surfactant Scavenging by Microbubble Clouds: Consequences for Capillary Wave Damping

Andrew J. Szeri[1], Ryan L. Stefan[2], and John R. Saylor[3]

[1] University of California at Berkeley, Berkeley, CA 94720–1740
[2] Science Applications International Corporation, San Diego, CA 92121–1578
[3] Naval Research Laboratory, Washington, DC 20375–5351

Abstract. Soluble surfactants adsorb to rising clouds of micro-bubbles and are subsequently deposited on the surface of the bulk liquid. The adsorbed surfactant leads to strongly increased damping of capillary waves, when compared to the damping rate of capillary waves on a clean surface. A theory is developed for the nonlinear dynamics of a bubble cloud, surfactant scavenging, and capillary wave damping. The main ingredients are: (i) an understanding of the connections between spatial structure in the bubble cloud and its mixing properties, deduced from numerical simulation and scaling analysis, (ii) horizontally averaged equations for the surfactant dynamics, and (iii) a (complex) dispersion relation that connects surface properties modified by the presence of surfactants to capillary wave damping.

1 Introduction

Surfactants are substances which find it energetically favorable to become closely associated with interfaces between, in this case, air and water. Dilute clouds of rising bubbles scavenge soluble surfactants that are subsequently deposited on the bulk interface of bodies of water [26–28,3]. In this paper, we study surfactant scavenging together with one of its main consequences: capillary wave damping.

In the scavenging problem, surfactant in the bulk adsorbs to (and desorbs from) the surfaces of the rising bubbles. When the bubbles reach the bulk surface, they donate their associated surfactant. One very important consequence is that capillary waves on the bulk surface are much more strongly damped than they would be on a clean surface. This happens due to a change in the hydrodynamic boundary condition associated with the presence of surfactants. Some recent experiments have shown that this mechanism is responsible for the surface slicks that are commonly observed behind ships at sea [21,19]. Typical bubble clouds of interest consist of dilute suspensions of bubbles in the size range of tens of μm; larger bubbles rise out of solution too quickly to be of much consequence, and smaller bubbles dissolve too quickly. The bubbles are formed in the wake of ships by the breaking of bow and stern waves, then carried deep under the surface by turbulence in the wake. The wake turbulence dies out much more rapidly than the bubbles rise out of suspension.

J.L. Lumley (Ed.): LNP 566, pp. 337–352, 2001.

In this paper, we begin by developing a computational model of a cloud of rising bubbles. The spatial distribution of bubbles in the cloud must have a very special structure in order to render convergent averages of rise speed and vertical velocity fluctuations induced in the water. We develop an effective diffusivity for the bubble-induced mixing (in the vertical) of surfactant dissolved in the bulk liquid, which is of great importance in solving the surfactant transport problem. Next, we consider bulk surface enrichment of surfactant by micro-bubble scavenging of dissolved surfactant. Finally, we examine the increase in capillary wave damping associated with the presence of surfactant.

2 Bubble cloud dynamics

Here we consider a monodisperse cloud of small bubbles; we neglect gas transfer between the bubbles and the surrounding liquid, and the fluid hydrostatic pressure variation during rise. The main ingredients of a bubble cloud model, to be discussed in turn, are as follows. The individual bubbles are approximated by fundamental solutions of the Stokes equations. The bulk surface is accounted for with an image system: a descending "anti-bubble" above the bulk surface for each bubble rising toward the bulk surface. The initial distribution of bubbles is assumed random at small length scales, but more homogeneous than random at longer length scales. Bubbles in the far field are accounted for using a mean field approach. The details are developed in the dissertation of Stefan [29], Chapters 1–4.

The Reynolds number, defined as $Re = U_0 a/\nu$, is assumed small. Here a is the bubble radius, U_0 is the rise speed, and ν is the kinematic viscosity. The steady Stokes equations describe the fluid motion. The fluid velocity is $\boldsymbol{u}$; the static pressure is P. The solution of interest about a rigid sphere is well known in spherical polar coordinates:

$$\frac{u_r}{U_0} = \frac{1}{2}\left[\frac{3a}{r} - \left(\frac{a}{r}\right)^3\right]\cos\theta, \quad \frac{u_\theta}{U_0} = \frac{1}{4}\left[\frac{3a}{r} + \left(\frac{a}{r}\right)^3\right]\sin\theta. \tag{1}$$

Here $U_0 = 2ga^2(\rho_f - \rho_b)/(9\mu)$ is the rise speed, u_r and u_θ are the radial and angular velocity components of the fluid, r is the radial coordinate measured from the bubble center, θ is the angle measured from U_0, ρ_f is the fluid density, ρ_b is the bubble density, g is the gravitational constant, and μ is the viscosity. A simpler model results if one instead makes use of a fundamental solution of the Stokes equations known as a stokeslet. This exerts the same force on the fluid and thus has the same rise speed U_0. The flow field is given by (1) without the terms proportional to $(a/r)^3$. As long as $(a/r) \ll 1$, as happens in the dilute cloud of present interest, the stokeslet approximation is satisfactory. We shall make use of the latter approximation in what follows.

2.1 Hydrodynamic interaction

When a cloud of bubbles rises through a viscous fluid, each bubble affects the motion of surrounding bubbles through its buoyancy-induced contribution to the flow field. The resultant velocity of a test bubble simply consists of its own velocity U_0, superimposed on the components induced from all other bubbles. The position of each bubble in the cloud can then be updated by integrating the expressions for the bubble velocities. Note that we make use of Faxen's correction as the bubbles are now regarded as moving through a fluid with spatially-varying background velocity [10].

Solutions for multi-body interaction, against which we have compared the straightforward technique just described, are available only for simple arrangements of a few settling spheres. Goldman, et al. [8] provide an exact solution for two settling spheres of equal size. For a sphere separation of only five radii, our pair-wise added stokeslets approximation differs from their exact solution only by about 1%. Accuracy improves with larger sphere separation. Ganatos, et al. [7] developed a highly accurate numerical solution for full multi-body hydrodynamic interaction for an instantaneous arrangement of spheres settling in vertical and horizontal chains. We made comparisons of the vertical velocity for chains containing 3, 5, and 9 spheres, separated from one another by only 4 radii. Our solution deviates from the more accurate solution by Ganatos, et al. by only a few percent. More accurate but far more computationally intensive methods have been developed for these problems [2].

2.2 The free surface

In order to account for the free surface, we employ an image stokeslet above the free surface, with opposite orientation, associated with each rising bubble. Because the stokeslet and its image are equal and opposite, there is no net force on the fluid. Far away, the bubble-image pair induces a fluid velocity that decays like r^{-2} instead of r^{-1}; we refer the reader to [17] for a clear discussion. This more rapid decay of the disturbance velocity of the bubble-image pair relative to a lone bubble has the effect of rendering convergent the average rise velocity of the bubbles. This is important, as it is well known that in a dilute, unbounded homogeneous suspension of monodisperse spheres, one obtains divergent integrals in a naive approach when determining the mean sedimentation speed of the particles. This divergence problem was overcome by Batchelor [1], who made use of a renormalization argument, and later by Hinch [12] and Feuillebois [5]. As a consequence of the image system, all points on the free surface have zero point-wise vertical velocity (but may have non-zero horizontal components) and zero shear stress in the plane of the surface.

2.3 Cloud structure and its evolution

A second instance of divergent averages must now be addressed with attention to the structure of the bubble cloud. The variance of the sedimentation speed of the particles of a random suspension grows without bound as the size of the sample (or volume) of the suspension increases [4]. Similarly, divergent integrals result from a calculation of tracer point diffusivity from a random array of point forces [15].

Cloud structure can be expected to play an important role in the dynamics of the suspension. Batchelor [1] showed that a random array of particles settles as $< U_z > /U_0 = 1 - 6.55\phi$; Hasimoto [11] showed that a precisely spatially periodic array of particles settles as $< U_z > /U_0 = 1 - 1.76\phi^{1/3}$. Here $\phi = (4\pi/3)a^3 n$ is the volume fraction of spheres. Saffman [22] describes the reasons for these differences in rise speed.

Koch and Shaqfeh [16] realized what is necessary to overcome the problem of divergent variance of velocity fluctuations: screening of hydrodynamic interactions. They observed that in a suspension in which there is a deficit of exactly one particle in a finite neighborhood of a marked particle, the velocity induced by that marked particle decays faster than (a/r) outside the neighborhood. We have realized that such a property is readily set up with the following initial arrangement, which we refer to as a single-cell random bubble cloud. Let n be the average number density of bubbles in the cloud (per unit volume). Space is discretized into cubical boxes of side $n^{-1/3}$, and one bubble is placed at a random location in each box. No two boxes are the same. There is no assumption of periodicity. This condition is only set at the initial time —the bubbles are in no way constrained thereafter. To understand why the single-cell random cloud structure persists in time, one can examine the conservation equation for the probability density of the positions of a group of N particles [16]. Because the dynamical system is divergence-free, an initially uniform probability density is simply convected around —thus remaining uniform.

The relative likelihood of finding a bubble at any point is identical in single-cell and truly random bubble clouds. The difference is that on length scales larger than the box size, the single-cell random distribution is more homogeneous than truly random. Moreover, it is easily shown that the single-cell random distribution has the required deficit of one bubble in the neighborhood of a marked bubble. The velocity variance is convergent as the size of the domain increases, and one can compute an effective diffusivity of bubble-induced mixing [31].

2.4 Mean field approach for bubbles in the far field

As a final component of the model, we describe briefly how bubbles in the far field are taken into account. In the mean field approximation, we augment the background velocity at a bubble location with an integral over the (uniform,

homogenized) density of bubbles in the far field. Because we treat the near field and far field differently, the bubble cloud domain is divided into two regions: the discrete region and the continuum region. The purpose of the continuum region is to provide the correct boundary condition for the discrete region. We take the discrete region to be a rectangular box of square plan form residing below the free surface surrounded by continuum. The discrete region need not be in contact with the free surface or with the bottom of the bubble cloud.

2.5 Average rise speed

It is possible to determine analytically the average vertical velocities of bubbles and fluid if one considers the entire domain outside a test bubble to be a continuum. In this case the continuum extends from the nearest-neighbor radius to infinity, and no bubble is allowed to overlap the bubble of interest.

For bubbles far from the surface, the average rise speed determined in this way is $< U_z > /U_0 = 1 - 5\phi$. This is the same expression obtained using the renormalization technique [1], excluding (as we do) the effect of reflections beyond the first.

For a single-cell random bubble cloud an analytical expression is more difficult to obtain because the bubble number density is more homogeneous than a truly random distribution at larger length scales. We must instead resort to a numerical simulation far from the free surface. Numerical results show that the average bubble rise speed is $< U_z > /U_0 = 1 - 1.27\phi^{-1/3}$. The average bubble rise speed for the single-cell random distribution thus lies between that of a perfectly periodic array and of a purely random distribution.

2.6 Velocity fluctuations induced by rising bubbles

Next we consider vertical velocity fluctuations. In [4] the variance in bubble vertical velocity diverges $\propto N^{1/3}$ for a large number of bubbles in a random distribution; our calculations agree. The standard deviation of the vertical component of fluid velocity is $u_{z,sd}$. The values for $u_{z,sd}$ in the random case diverge, but those for the single-cell random bubble distribution do not.

In Fig. 1 we show a typical normalized PDF of vertical velocity fluctuations in the fluid far from the free surface. The overall shape of the distribution is nearly Gaussian. The width and the severity of skewness are both functions of the bubble volume fraction and depth.

The roughly Gaussian nature of the vertical velocity distribution justifies our focus on the velocity variance. We find that far below the surface, fluid and bubble vertical velocity standard deviations follow

$$\frac{u_{z,sd}}{U_0} = 1.5\phi^{1/3} \tag{2}$$

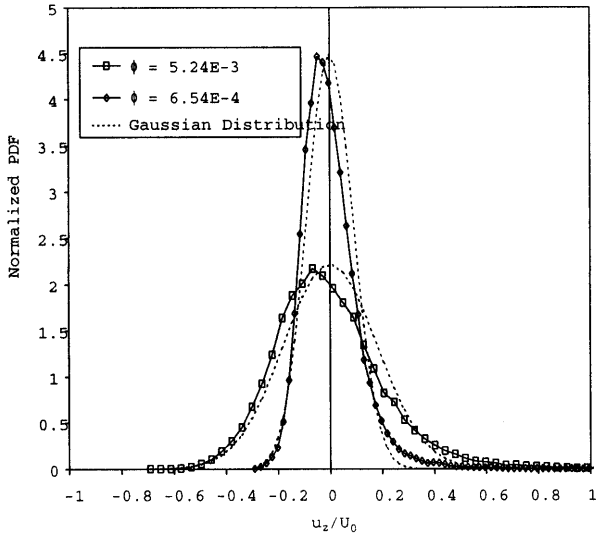

Fig. 1. Normalized PDF of fluid point (and bubble) dimensionless vertical velocity u_z/U_0 for different bubble volume fractions ϕ far from the free surface in a single-cell random bubble cloud. The results represent averages of 500 initial bubble cloud realizations

to about $\phi \approx 0.05$. Koch and Shaqfeh [16] argue $(u_{z,sd}/U_0)^2 \approx \phi R_s/a$ in a homogeneous suspension of sedimenting spheres, where R_s is the screening distance. In a single-cell random cloud $R_s/a \propto \phi^{-1/3}$ (see 2.3), hence (2) is consistent with their result.

The free surface is found to have an influence on the fluid vertical velocity fluctuations as illustrated in the correlation of vertical velocity standard deviation with depth [31]:

$$\frac{u_{z,sd}}{1.5U_0\phi^{1/3}} = \frac{A(\phi)|z^*|}{1 + A(\phi)|z^*|},$$

where $A(\phi) = 0.891\,\phi^{0.212}$ and $z^* = z/a$. More concentrated bubble clouds mix the fluid more vigorously at depth, and carry that more vigorous mixing closer to the surface.

2.7 Fluid mixing

The goal of the bubble cloud model is to develop an effective diffusivity for the vertical mixing process. Koch [13] determines the rate $\propto N^{1/2}$ at which the diffusivity grows with the number N of random sedimenting particles in a periodic box. He concludes that the diffusion (in that case) is dominated

by convective motions occurring on the scale of the box size. In the case of a single-cell random distribution, the diffusivity is convergent.

We begin the development of an effective diffusivity far below the surface, by following an evolving cloud of fluid tracer points with time. The effective diffusivity is related to the rate of spread of tracer points through $D^{\infty}_{eff} = \sigma^2/(2t)$. Care is taken in measuring the standard deviation σ at times when the fluid point motion is no longer self-correlated. In the calculations we approximate true bubble-bubble hydrodynamic interaction with its mean effect; namely, by having the bubbles rise at their average speed due to hydrodynamic interaction with zero horizontal velocity. This increases the residence time a passing bubble has with a neighboring fluid point, which induces more fluid point mixing. Numerical results are shown in Fig 2. The eddy diffusivity ϵ includes molecular diffusivity as well.

Following [14], we estimate the dimensionless eddy diffusivity $\epsilon^{\infty}_{HI}/(U_0 a)$ as the product of the rate at which a tracer point undergoes interaction with a nearby bubble-image pair, R, times the mean square vertical displacement caused by such an interaction. By nearby, we mean, say, within the box defined in section 2.3; this is related to the cloud structure. On average, there is one bubble within such a distance, which rises through the neighborhood over a time proportional to $a\phi^{-1/3}/U_0$; hence $R \propto U_0\phi^{1/3}/a$.

The square of the vertical displacement caused by an interaction is conveniently obtained numerically by integrating the motion of a tracer point while it is within a distance $n^{-1/3}/2$ of a bubble rising at the mean speed. This is subsequently averaged over the neighborhood of the tracer point, as the next interacting bubble could appear with equal probability anywhere within the neighborhood. Because this is just a scaling argument, we obtain the multiplicative constant (0.2 in this case) by best matching the data with the result of the scaling argument. A convenient formula (nearly identical to the scaling law) is

$$\frac{\epsilon^{\infty}_{HI}}{U_0 a} = \frac{\phi^{\gamma}}{1 - \zeta\phi^{\xi}}, \tag{3}$$

where $\gamma = 0.327534$, $\zeta = 1.2601$ and $\xi = 0.0948548$; this is shown in Fig. 2, along with the results of simulations.

There is no need to modify the scaling argument just described for points at a finite distance from the free surface. All that changes is that the vertical displacement of a tracer particle is reduced as a consequence of the proximity of the image bubble. The way in which the eddy diffusivity decreases as one approaches the surface, made dimensionless by its value at great depth, is shown in Fig. 3. We emphasize that the same scaling law was used to obtain Figs. 2 and 3. A convenient formula is (to $\phi \approx 0.006$):

$$\frac{\epsilon_{HI}(z^*)}{\epsilon^{\infty}_{HI}} = \frac{\eta(\phi)}{1 + \eta(\phi)}, \tag{4}$$

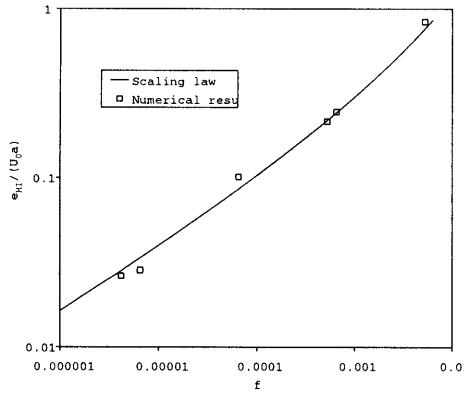

Fig. 2. Comparison of the scaling law (3) and numerical data for the dimensionless eddy diffusivity $\epsilon_{HI}^{\infty}/(U_0 a)$ far below the surface as a function of the volume fraction ϕ

where $\eta(\phi) = 0.144053\phi^{1/2} - 1.09454\phi$. The root mean square vertical displacement of tracer points associated with an interaction with a rising bubble is always much less than the depth of the tracer points. This ensures that a local description of the transport in terms of a diffusivity is valid [14].

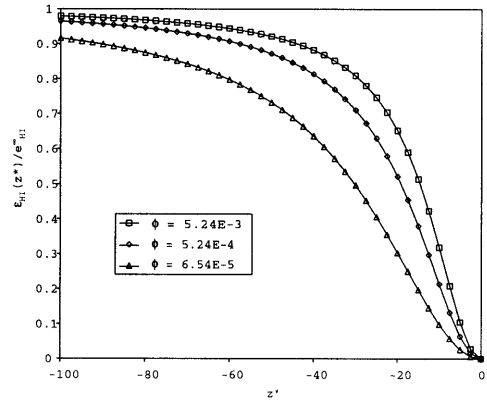

Fig. 3. Dimensionless eddy diffusivity $\epsilon_{HI}(z^*)/\epsilon_{HI}^{\infty}$ as a function of dimensionless depth z^* below the surface

Finally, we show in Fig. 4 the results of a strong test of the depth-dependent effective diffusivity. Tracer points are released just below the sur-

face ($z = -0.05$ cm), where the eddy diffusivity is most rapidly changing, and allowed to spread due to the rise of a cloud of 50 μm bubbles with $\phi = 0.00524$ for 0.8 s. In the figure we show the normalized PDFs of tracer particle depths; the asymmetry of the PDFs is a consequence of the depth-dependence of the mixing. A secondary effect is related to the skewness found in the vertical velocity PDFs (see Fig. 1). The two curves correspond to the result of a bubble cloud simulation, and that of a finite difference calculation of the time-dependent diffusion equation employing the depth-dependent effective diffusivity obtained from the scaling analysis. The comparison is quite satisfactory considering the fits of the scaling analysis spans four orders of magnitude in ϕ, and the diffusivity in this problem varies by more than two orders of magnitude across the domain. Other tests gave similar results.

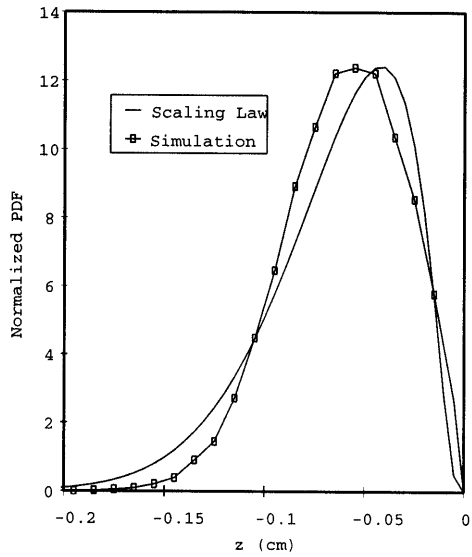

Fig. 4. PDF of tracer particle depths at 0.8 s. Particles were initially released in a plane at $z = -0.05$ cm. The simulation results represent the average of 500 initial bubble cloud realizations; each bubble cloud consisted of 50 μm bubbles with $\phi = 0.00524$. The effective diffusivity over the domain varies by more than two orders of magnitude

Unfortunately, there is little in the way of experimental data to which we can compare. But we now discuss some results that are roughly comparable. Nicolai, et al. [20] did make various measurements of properties in a settling suspension at $\phi = 0.05$, but nothing is known of the structure of their suspension. They found $u_{z,sd}/U_0 = 0.62 \pm 0.08$, whereas our correlation yields

$u_{z,sd}/U_0 = 0.55$. Koch and Shaqfeh by comparison predict $u_{z,sd}/U_0 = 2.2$ in a spontaneously screened suspension. Nicolai, et al. measured the vertical self-diffusivity of the particles to be $\epsilon^{\infty}_{HI}/U_0 a = 5$ (6 for [9]); our correlation yields 7.3 for tracer point diffusivity, and Koch and Shaqfeh determine 10.4. The self-diffusivity of bubbles would be a little smaller than our tracer point diffusivity of 7.3. We note that Nicolai, et al. find $\epsilon^{\infty}_{HI}/U_0 a$ decreases with ϕ at larger concentrations —this they attribute to the collective motion of small clusters of particles. Such an effect is beyond the scope of the present work.

In a very recent series of experiments, Segrè, et al. [25] undertook a detailed examination of suspension structure during sedimentation. They found $(u_{z,sd}/U_0) \propto \phi^{1/3}$. Segrè, et al. also determined a lengthscale from the spatial correlation of the vertical component of velocity fluctuations to be $\xi \propto a\phi^{-1/3}$. Our suspension exhibits the same scaling as a consequence of the distribution we assume. In their model, the correlation lengthscale ξ is the cutoff length beyond which particles are no longer randomly distributed —as we have shown, this is the screening length. No experiments have addressed the variations in properties near a free surface.

3 Surfactant scavenging

We are interested primarily in the average steady-state behavior of surfactant transport within a horizontally large bubble cloud; however, fluctuations from average quantities also play a role. As bubbles rise, fluctuations in fluid velocity will induce fluctuations in bubble rise speed, bubble number density, bulk surfactant concentration, bubble-surface concentration of surfactant, and bulk-surface concentration of surfactant. In keeping with the assumptions established for the effective diffusivity of a single-cell random distribution of bubbles we assume that the bubble number density and bubble velocity have negligible fluctuating components. We do, however, allow fluctuations in bulk fluid velocity, bulk surfactant concentration, bulk-surface concentration of surfactant, and bubble-surface concentration of surfactant.

There are several kinetic models that describe adsorption and desorption of surfactants. In general, the rate of adsorption depends on the nearby bulk concentration of surfactant, and on the population already resident at the interface. The rate of desorption normally depends only on the population on the interface. Nonlinear saturation yields a maximum surface concentration, or surface-excess, of surfactants that can populate an interface. In the bulk fluid, surfactant molecules convect and diffuse, although the latter with low mobility due to the large sizes of these molecules.

The equations are developed in [30], along with a scheme for horizontal averaging and an analysis of terms involving averages of products of fluctuation quantities. The latter are shown to be negligible as a consequence of the separation of time scales for convection and surfactant kinetics.

The steady-state transport equation for the (horizontally averaged) bulk concentration of surfactant $\bar{c}(z)$ is

$$\frac{\mathrm{d}}{\mathrm{d}z}\left(\epsilon_{HI}(z)\frac{\mathrm{d}\bar{c}(z)}{\mathrm{d}z}\right) - 4\pi a^2 n\bar{q}_b(z) = 0. \tag{5}$$

Here

$$\bar{q}_b(z) = \alpha\left[\bar{c}(z)\left(\gamma_{sat} - \bar{\gamma}_b(z)\right) - \frac{\bar{\gamma}_b(z)}{\beta}\right]$$

represents the average flux of surfactant, from the bulk liquid to the bubbles, at depth z. This term accounts for (Langmuir) surfactant kinetics through the adsorption rate constant α and the desorption rate constant β. Typical values for these constants are in the range $10^7\,\mathrm{cm}^3/(\mathrm{gmol\,sec})$ and $10^7\,\mathrm{cm}^3/\mathrm{gmol}$, respectively. A typical bulk concentration of surfactant is $10^{-7}\,\mathrm{gmol/cm}^3$. A representative saturation concentration of surfactant on a surface is $\gamma = 5\times10^{-10}\,\mathrm{gmol/cm}^2$. A typical bubble size of interest is $50\,\mu\mathrm{m}$.

In order to determine the boundary condition at the bulk surface, we assume that adsorption/desorption at the bulk surface is also described by Langmuir kinetics and apply the same decomposition into mean and fluctuating components. The flux of surfactant from the bulk liquid to the bulk surface is

$$\bar{q}_s = \alpha\left[\bar{c}(0)\left(\gamma_{sat} - \bar{\gamma}_s\right) - \frac{\bar{\gamma}_s}{\beta}\right].$$

The boundary condition at the bulk surface is a balance between the flux of surfactant diffusing toward (or away) from the surface into the bulk and the flux of surfactant adsorbing to (or desorbing from) the surface:

$$-\epsilon_{HI}(0)\frac{\mathrm{d}\bar{c}(0)}{\mathrm{d}z} = \bar{q}_s. \tag{6}$$

The governing equation for the average steady-state surfactant concentration on the bubbles at depth z is,

$$\bar{u}_b\frac{\mathrm{d}\bar{\gamma}_b(z)}{\mathrm{d}z} = \bar{q}_b(z). \tag{7}$$

where $\bar{u}_b = U_0(1-1.27\phi^{1/3})(1+\phi)$ is the average bubble rise speed for a single-cell random distribution of bubbles adjusted to account for the upward flux of fluid and bubble volume from the bubble generation at the bottom of the bubble cloud. To determine the average steady-state surfactant concentration on the bulk surface we add the flux of surfactant from the bulk fluid to the flux of surfactant by bubbling. The result is,

$$\bar{q}_s + 4\pi a^2 n\bar{u}_b\bar{\gamma}_b(0) = 0. \tag{8}$$

Solved together, equations (5, 6, 7, 8) yield the averaged profiles with depth of the surfactant concentration resident on bubble surfaces and dissolved in the bulk liquid. The main result is the enrichment of surfactant

concentration on the bulk surface. Solution procedures for these nonlinear equations are outlined in [30].

A simple limiting case can be appreciated by examination of (8). Suppose bubbles arrive at the surface fully saturated with surfactant, and that the surface is fully saturated also; then (8) becomes

$$\frac{\alpha}{\beta} = 4\pi a^2 n_{max} \bar{u}_b.$$

Hence, the limiting number density of bubbles required to keep the bulk surface fully saturated is $n_{max} = \alpha/(4\pi a^2 \bar{u}_b \beta)$. For the typical parameter values we mentioned earlier, this yields $n_{max} = 6500\,\mathrm{cm}^{-3}$ or $\phi_{max} = 0.34\%$. Even in this limiting case, the bubble-induced mixing affects how long bubbles must rise in order to reach the surface fully saturated. When surface concentrations are less than saturation, the bubble-induced mixing determines what will be the enrichment of the bulk surface by bubbling [30].

Associated with the assumption of Langmuir kinetics, one can write down an expression for the surface pressure [6]

$$\pi = -RT\gamma_{sat} \ln(1 - \gamma_s/\gamma_{sat}), \tag{9}$$

where R is the gas constant and T is the temperature. The Gibbs surface elasticity for the same Langmuir kinetics is

$$E_0 = RT\gamma_s/(1 - \gamma_s/\gamma_{sat}). \tag{10}$$

These are required in the analysis of capillary wave damping, to which we now turn.

4 Capillary wave damping

Capillary wave damping associated with the presence of surfactants has been of considerable interest for some time. In [24] we present a review of the methods used for measuring capillary wave damping, as well as a description of new experiments and theory for a capillary wave damping experiment in a circular domain. The reason for exploration of a circular geometry rather than the usual rectangular geometry is the elimination of edge effects. In the experiments, the waves are produced by rapid (120 Hz) vertical vibrations of a cylindrical vessel. The capillary waves propagate in from the rim of the vessel, where there is a contact line, to the geometric center. There, they reflect. The superposition of the inward-traveling wave and the outward-traveling reflection creates a true standing wave only at the origin; otherwise, the wave is primarily inward-propagating as a consequence of geometric focusing and damping.

In [24], a theory for the amplitude of such waves was developed, without the usual restriction to distances far-removed from the origin. The theoretical amplitude curves for the wave slope were compared to data from a laser

slope gauge [23]. This allowed for the determination of the exponential damping factor as a function of surfactant surface concentration. The theory and experiment showed excellent agreement, as shown in Fig. 5.

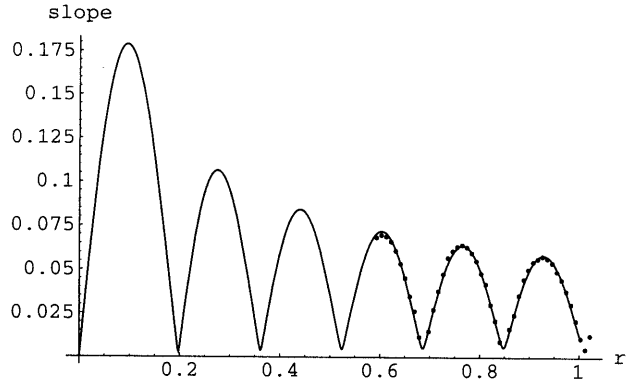

Fig. 5. Comparison of the theoretical curve and experimental data (points) for the amplitude of the slope (m/m versus r (cm) of time-dependent capillary waves in a cylindrical vessel. The surfactant is stearic acid, at a concentration of 0.1381 $\mu g/cm^2$

The wavelength and decay rate of capillary waves is related to the Gibbs elasticity E_0 and surface tension $\sigma = \sigma_0 - \pi$ through a dispersion relation. The latter derives from a solvability criterion that stems from the boundary conditions associated with normal and shear stresses at the interface. The dispersion relation developed in [24], without the far-field approximation, is the same for plane and for circular waves. At frequencies greater than about 1 Hz, the dispersion relation is the same for soluble and insoluble surfactants [18].

The surfactants considered in [24] were stearic acid, oleyl alcohol and hemicyanine —all insoluble. However, we can get an idea of how sensitively capillary wave damping depends on surface concentration of surfactant by examination of the data for these insoluble surfactants, as the mechanics of damping is the same for high enough frequencies [18]. For stearic acid, Saylor, et al. [24] find that an increase of surface concentration from 0.1 $\mu g/cm^2$ to 0.27 $\mu g/cm^2$ results in a change in the decay rate of waves from 0.12 cm^{-1} to 0.55 cm^{-1}. In a soluble surfactant system governed by Langmuir kinetics, given $\gamma_{max} = 10 \times 10^{-10}$ gmol/cm^2 and $T = 20$ C, one finds through the use of (9,10) and the dispersion relation [24] that a bulk surface enrichment of $\gamma_s = 1 \times 10^{-10}$ gmol/cm^2 to $\gamma_s = 7 \times 10^{-10}$ gmol/cm^2 leads to a comparable change in the decay rate of waves from 0.15 cm^{-1} to 0.51 cm^{-1}. In Fig. 6, we show the decay of two one-dimensional waves for comparison. The volume fraction of the bubble cloud required to enhance the surface-excess to $\gamma_s = 7 \times 10^{-10}$ gmol/cm^2 is readily computed [30]. In any case it is certainly less

than $\phi_{max} = 0.34\%$, in the case of the typical parameter values we mentioned earlier.

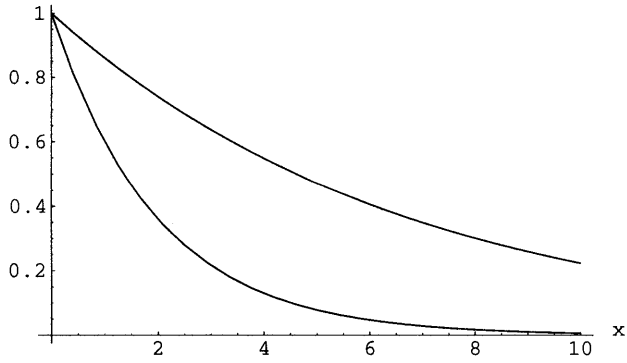

Fig. 6. Comparison of the amplitude decay with position x (cm) of two different planar capillary waves, with decay rates corresponding to 10% and 70% of saturation for the model surfactant. The slowly decaying wave has decay rate $0.15\,\mathrm{cm}^{-1}$; the rapidly decaying wave has decay rate $0.51\,\mathrm{cm}^{-1}$

5 Conclusions

In this paper we presented a theory for enhanced capillary wave damping which is associated with surfactant scavenged by a rising cloud of microbubbles. The surface enrichment by deposition of surfactant scavenged from the bulk depends sensitively on the mixing properties of the cloud. The rising bubbles mix the fluid vigorously at depth, but in a way which declines dramatically as the bulk surface is approached. A scaling model was developed for the effective diffusivity of the vertical mixing, in concert with numerical simulation of cloud dynamics.

An enrichment of the surface concentration of surfactant by scavenging results in decreased surface tension and increased surface elasticity. Through the dispersion relation for capillary waves, these changes are connected to an increase in the damping of capillary waves.

This work was supported by the Office of Naval Research under the Young Investigator and AASERT programs, and through the Naval Research Laboratory.

References

1. Batchelor, G.K. (1972) Sedimentation in a dilute dispersion of spheres. J. Fluid Mech. **52**, 245–268
2. Brady, J. F., Bossis, G. (1988) Stokesian dynamics. Ann. Rev. Fluid Mech. **20**, 111–157
3. Brown, J. W., Skop, R. A., Viechnicki, J., Tseng, R.-S. (1992) Transport of surface-active organic materials from sea water to the air-water interface by an ascending current field. Fluid Dyn. Res. **9**, 97–105
4. Caflisch, R. E., Luke, J. H. C. (1985) Variance in the sedimentation speed of a suspension. Phys. Fluids **28**, 759–760
5. Feuillebois, F. (1984) Sedimentation in a dispersion with vertical inhomogeneities. J. Fluid Mech. **139**, 145–171
6. Edwards, D. A., Brenner, H. and Wasan, D. T. (1991) Interfacial transport processes and rheology. Butterworth-Heinemann, Boston
7. Ganatos, P. , Pfeffer, R., Weinbaum, S. (1978) A numerical-solution technique for three-dimensional Stokes flows, with application to the motion of strongly interacting spheres in a plane. J. Fluid Mech. **84**, 79-111
8. Goldman, A. J., Cox, R. G., Brenner, H. (1966) The slow motion of two identical arbitrarily oriented spheres through a viscous fluid. Chem. Eng. Sci. **21**, 1151–1170
9. Ham, J. M., Homsy, G. M. (1988) Hindered settling and hydrodynamic dispersion in quiescent sedimenting suspensions. Int. J. Multiphase Flow **14**, 533–546
10. Happel, J., Brenner, H. (1973) Low Reynolds Number Hydrodynamics. Kluwer Academic Publishers
11. Hasimoto, H. (1959) On the periodic fundamental solutions of the Stokes equation and their application to viscous flow past a cubic array of spheres. J. Fluid Mech. **5**, 317–328
12. Hinch, E. J. (1977) An averaged-equation approach to particle interactions in a fluid suspension. J. Fluid Mech. **83**, 695–720
13. Koch, D. L. (1994) Hydrodynamic diffusivity in a suspension of sedimenting point particles with periodic boundary conditions. Phys. Fluids **6**, 2894–2900
14. Koch, D. L. (1996) Hydrodynamic diffusion near solid boundaries with applications to heat and mass transport into sheared suspensions and fixed-fiber beds. J. Fluid Mech. **318**, 31–47
15. Koch, D. L., Brady, J. F. (1985) Dispersion in fixed beds. J. Fluid Mech. **154**, 399–427
16. Koch, D. L., Shaqfeh, E. S. G. (1991) Screening in sedimenting suspensions. J. Fluid Mech. **244**, 275-303
17. Leal, L. G. (1992) Laminar Flow and Convective Transport Processes. Butterworth-Heinemann
18. Lucassen, J., Hansen, R. S. (1967) Damping of waves on monolayer-covered surfaces. II. Influence of bulk-to-surface diffusional interchange on ripple characteristics. J. Colloid Int. Sci. **23**, 319–328
19. Milgram, J. H., Peltzer, R. D., Griffin, O. M. (1993) Suppression of short sea waves in ship wakes: measurements and observations. J. Geophys. Res. **98**C, 7103–7114.
20. Nicolai, H., Herzhaft, B., Hinch, E. J., Oger, L., Guazzelli, E. (1995) Particle velocity fluctuations and hydrodynamic self-diffusion of sedimenting non-Brownian spheres. Phys. Fluids **7**, 12–23

21. Peltzer, R. D., Griffin, O. M., Barger, W. R., Kaiser, J. A. C. (1992) High-resolution measurement of surface-active film redistribution in ship wakes. J. Geophys. Res. **97**C, 5231–5252.
22. Saffman, P. G. (1973) On the settling speed of free and fixed suspensions. Stud. Appl. Math. **52**, 115–127
23. Saylor, J. R., Handler, R. A. (1997) Gas transport across an air/water interface populated with capillary waves. Phys. Fluids **9**, 2529–2541
24. Saylor, J. R., Szeri, A. J., Foulks, G. P. (1999) Measurement of surfactant properties using a standing, circular capillary wave field. In review
25. Segrè, P. N., Herbolzheimer, E., Chaikin, P. M. (1997) Long-range correlations in sedimentation. Phys. Rev. Lett. **79**, 2574–2577
26. Skop, R. A., Brown, J. W., Ramberg, S. E. (1989) Adaptation of a digital nuclear imaging technique for the study of bubble scavenging of surface-active organic materials in sea water. Exp. Fluids **7**, 429–431
27. Skop, R. A., Lindsley, W. G., Brown, J. W. (1991) Radiotracer studies of surfactant transport to the sea-air interface by sub-millimeter-size bubbles. Exp. Fluids **10**, 251–256
28. Skop, R. A., Viechnicki, J. T., Brown, J. W. (1994) A model for microbubble scavenging of surface-active lipid molecules from sea water, J. Geophys. Res. **99**C, 16395–16402
29. Stefan, R. L. (1997) Bubble-induced mixing and surfactant transport near a free surface. U. C. Irvine Ph.D. Dissertation
30. Stefan, R. L., Szeri, A. J. (1999) Surfactant scavenging and surface deposition by rising bubbles. J. Colloid Int. Sci. **212**, 1–13
31. Stefan, R. L., Szeri, A. J. (1999) Bubble-induced mixing near a free surface. In review